Advanced Materials Technologies

ADVANCED MATERIALS TECHNOLOGIES
www.advmattechnol.com

RESEARCH ARTICLE

Multimodal Physiological Sensor Based Smart Wristband: Real-Time Monitoring of Physical Activity and Muscle Fatigue

Daiwu Shen[1,2] | Puchuan Tan[2] | Yang Zou[3,4] | Yuan Xi[2,5] | Cong Li[2,6] | Aihua Liang[6] | Guanlin Liu[1] | Zhou Li[3,4]

[1]Center on Nanoenergy Research, institute of Science and Technology for Carbon Peak & Neutrality, School of Physical Science & Technology, Guangxi University, Nanning, China | [2]Beijing Institute of Nanoenergy and Nanosystems, Chinese Academy of Sciences, Beijing, P. R. China | [3]School of Clinical Medicine, Tsinghua Changgung Hospital, Tsinghua University, Beijing, P. R. China | [4]School of Biomedical Engineering, Tsinghua University, Beijing, P. R. China | [5]Key Laboratory of Biomechanics and Mechanobiology of Ministry of Education Advanced Innovation Center For Biomedical Engineering School of Engineering Medicine, Beihang University, Beijing, P. R. China | [6]State Key Laboratory for Quality Ensurance and Sustainable Use of Dao-di Herbs, Institute of Chinese Materia Medica, China Academy of Chinese Medical Sciences, Beijing, P. R. China

Correspondence: Puchuan Tan (tanpuchuan@binn.cas.cn) | Guanlin Liu (guanlinliu@foxmail.com) | Zhou Li (li_zhou@tsinghua.edu.cn)

Received: 17 September 2025 | **Revised:** 15 December 2025 | **Accepted:** 4 January 2026

Keywords: artificial intelligence| hybrid sensor| muscle fatigue monitoring| multimodal physiological sensor| physical activity monitoring

ABSTRACT

The growing prominence of personal health issues has made appropriate physical exercise increasingly essential for maintaining health. To ensure adequate workout while preventing overexertion, reliable exercise intensity assessment methods are crucial. However, existing approaches suffer from operational complexity and failure to account for individual physiological differences. In this paper, a multimodal exercise intensity monitoring wristband integrating piezoelectric, thermoelectric, and electromyography technologies is developed. A PVDF-based piezoelectric sensor is employed to monitor pulse. $Bi_{0.5}Sb_{1.5}Te_3$ and $Bi_2Se_{0.3}Te_{2.7}$ thermoelectric legs are selected to fabricate a thermoelectric sensor for body temperature monitoring, and sEMG is used for muscle fatigue assessment. These physiological signals (pulse, body temperature, and muscle fatigue) enable effective exercise intensity evaluation. During continuous exercise, it is achieved continuous monitoring of heart rate, body temperature, and sEMG of the subject. Specifically, the subject's heart rate increased from 77.60 to 91.04 bpm, body temperature rose from 35.3 to 36.0°C, and the continuous changes in sEMG are also recorded. Then, through machine learning algorithms, quantitative relationships are established between signal feature value and exercise intensity levels, generating personalized exercise recommendations. This research demonstrates significant potential for applications in intelligent and personalized physiological health monitoring systems.

1 | Introduction

Under the global context of rapid technological advancement, individual physical health status has become a prominent concern. The current accelerated pace of life and work leaves insufficient time for regular exercise, coupled with widespread inadequate physical activity levels. Prolonged energy intake exceeding expenditure predisposes individuals to obesity [1], thereby significantly increasing risks of developing type 2 diabetes [2, 3], hypertension [4–6], fatty liver disease [7, 8], and

Daiwu Shen and Puchuan Tan contributed equally to this work.

other metabolic disorders [9, 10]. Growing awareness recognizes physical exercise as essential for maintaining health. Appropriate exercise modalities and intensity critically determine workout efficacy. Suboptimal exercise volume leads to inadequate energy expenditure, negating training benefits. Conversely, excessive exercise may induce adverse reactions such as dehydration and chest tightness, while also exacerbating cardiac strain [11] and joint degeneration [12–14]. Evidence-based assessment of exercise volume provides scientific guidance for physical training, ensuring achievement of energy expenditure targets while preventing exercise-related injuries [15].

Traditional exercise volume assessment methodologies can be categorized into subjective approaches (behavioral observation and questionnaire surveys) and objective techniques (respiratory calorimetry and doubly labeled water method) [16]. While behavioral observation and questionnaires effectively evaluate exercise intensity and volume, their reliability is compromised by observer bias and athletes' subjective perceptions, failing to establish accurate quantitative assessments. Objective methods employ physiological signals acquisition through sensors, such as respiratory gas analysis and doubly labeled water techniques, which provide scientifically validated metrics for exercise intensity quantification, offering significant advantages over subjective evaluations in methodological rigor [17, 18]. However, these conventional objective approaches often require specialized equipment and operator expertise, limiting their real-time applicability and user-friendliness. Consequently, developing portable, highly integrated physiological signal sensors capable of capturing comprehensive biometric data presents a viable research direction for enhancing exercise assessment through improved accuracy, operational simplicity, and real-time monitoring capabilities.

Recent advancements in piezoelectric nanogenerators (PENGs) [19–22], triboelectric nanogenerators (TENGs) [23–27], and thermoelectric generators (TEGs) [28–32] have propelled their widespread adoption in wearable and implantable physiological signals sensing systems. Numerous studies leveraging these novel transducer technologies demonstrate significant potential for monitoring vital biomarkers including pulse waveforms, body temperature, blood pressure, and human kinematics, owing to their distinctive technical merits: 1) simple structure providing significant benefits for signal detection in confined spaces with enhanced integration feasibility [33–35]; 2) low power consumption enabling operation without external power supply [36–38]. Due to their self-powering capability [39, 40], integrating these devices into sensor systems to provide energy presents a promising solution to overcome the limitations of batteries and external power sources [41, 42]; 3) high sensitivity allowing responsive detection of subtle forces and temperature variations [43–47]. Existing implementations generally utilize single sensors that capture only one signal type. The absence of complementary signal modalities restricts both data volume and diversity, ultimately compromising assessment accuracy. This underscores the necessity for developing integrated multimodal sensors to acquire adequately comprehensive physiological signals.

Multimodal sensors enhance detection accuracy by aggregating heterogeneous physiological signals, enabling multi-angled assessment of physiological states through enriched information acquisition [43]. Under this strategy, various sensors are integrated in different combinations, complementing and enhancing each other. For instance, the simple structure of a thermosensitive/pressure-sensitive sensor based on a nanowire network demonstrates the potential of a single sensing element to respond to multiple types of signals [48]. The electrocardiogram and pulse-based multimodal sensor for cuffless blood pressure monitoring shows promising applications distinct from traditional blood pressure cuffs [49]. Additionally, the thin-film flow sensor with an asymmetric thermal structure accurately identifies the flow velocity and direction of fluids, providing a novel solution for fluid measurement in medical, industrial, and other fields [50].

In the field of personalized healthcare, various multimodal sensing systems have been developed to monitor physiological information such as sweat metabolites, respiratory parameters, and cardiovascular waveforms [36, 37, 51–53]. Current investigations focus on synergistic interpretation of cross-modal bio-signals to establish comprehensive physiological profiles. In a representative study, Dai et al. developed a polyvinylidene fluoride (PVDF) film-based sensor utilizing both piezoelectric and pyroelectric properties to concurrently detect pressure and temperature signals [37]. By integrating this with an acetone-specific gas sensor, the system achieved simultaneous monitoring of mechanical signals, temperature variations, and acetone molecular concentration during respiration. The synergistic analysis of these three parameters enhanced the accuracy of human respiratory monitoring. In sweat analysis research, Zhang et al. engineered a non-invasive multimodal sensor integrating sweat stimulation with sample collection [51]. This device operates by inducing sweat secretion through electrical stimulation while simultaneously monitoring biomarkers including uric acid, glucose, and lactate, along with pH fluctuations and skin surface temperature. The system effectively addresses conventional limitations such as invasive sampling methods, time-delayed detection, and single-parameter measurement constraints in physiological monitoring. These findings demonstrate multimodal sensors' capability to enhance sensing accuracy, improve system integration, and expand application scenarios. However, high-volume physiological signal acquisition imposes heightened requirements on data processing capacity. This necessitates employing machine learning techniques to extract physiologically relevant features from such voluminous, multi-dimensional datasets.

During exercise, as the intensity increases, various biomarkers typically change [54–57], such as heart rate [58], body temperature [59], sEMG [60], electroencephalography (EEG) [61, 62], electrocardiography (ECG) [63–65], blood pressure, respiration [66], and metabolic compounds [67, 68]. Among these, heart rate, body temperature, and surface electromyography reflect cardiovascular function, thermoregulation, and neuromuscular fatigue, respectively. Here, this paper proposes a multimodal exercise intensity assessment wristband (MEIAW) based on PENG, TEG, and surface electromyography (sEMG) that can simultaneously monitor these three signals. The obtained signals are sent to personal terminal by wireless transmission module and given reasonable exercise suggestions through machine learning. Research shows that evaluation accuracy using three-modal signals is significantly better than single-modal signal assessments, demonstrating that multimodal sensing solutions improve accuracy in personalized healthcare and health monitoring.

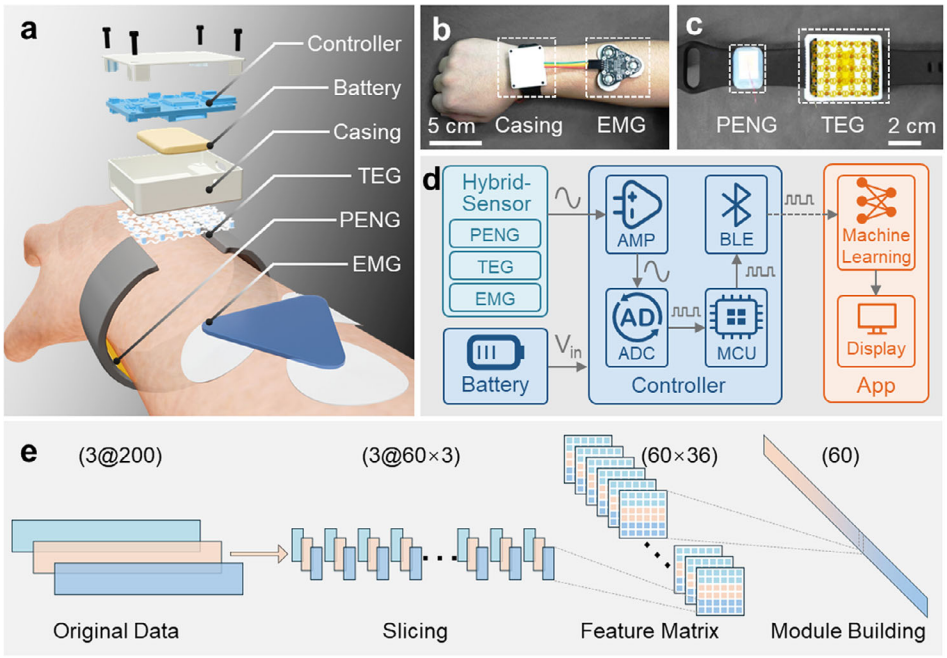

FIGURE 1 | Schematic diagram of multimodal exercise intensity monitoring wristband. (a) Schematic diagram of MEIAW structure. (b,c) are the physical image and wearing status of MEIAW, respectively. (d) Design concept of the sensing system. (e) Data processing and architecture design of the machine learning part.

2 | Result

The structural design of the MEIAW is shown in Figure 1a, consisting of five primary components: the PENG module, the TEG module, the sEMG module, the control module, and the power module. Here, the PENG is used to detect wrist pulse signals, the TEG is employed to monitor body temperature variations, and the sEMG is selected for collecting electrical signals generated by muscular activity. The wrist offers ideal anatomical advantages for deploying these sensors: its superficial radial artery exhibits minimal overlying tissue, facilitating clear pulse waveform capture; the wrist provides sufficient contact area to establish stable thermal gradients for the TEG sensor; proximity to forearm muscle groups enables accurate surface electromyography (sEMG) signal acquisition during wrist motion. During operation, PENG requires prestress application to match measurement range of the sensor. Consequently, the PENG sensor is positioned at the interface between the wristband and the radial artery. The wristband provides necessary preload while simultaneously, the radial artery location offers the clearest pulse signals and the most reliable acquisition process. TEG requires a large contact area for thermal signal acquisition to minimize environmental interference. Therefore, the TEG sensor is installed at the interface between the casing and wrist, where the largest and most complete contact area is achieved. To reduce the problem of motion artifacts during the electromyography acquisition process, the sEMG is deliberately placed on the outside of the entire device, adhered to the skin through wet electrodes, and connected to the control module via wires. In addition to these three modules, all other components are encapsulated within a 42 mm (L) × 32 mm (W) × 14 mm (H) 3D-printed enclosure fabricated from polyvinyl chloride (PVC). Figure 1b,c demonstrate the wearing posture of MEIAW and physical configuration, respectively.

The design concept is illustrated in Figure 1d. Three sensing modules (PENG, TEG, and sEMG) are responsible for acquiring physiological signals and transducing them into electrical signals. These raw signals are amplified via operational amplifiers. The amplified analog signals are then converted to digital signals through an analog-to-digital converter (ADC), enabling the microcontroller to detect real-time signal intensity. The average power consumption of MEIAW is approximately 185 mW; thus, a 400 mAh (≈1.32 Wh) lithium-ion battery is integrated. The whole system of MEIAW can operate continuously for at least 8 h, which sufficiently covers the entire duration of a typical exercise session. To facilitate exercise intensity monitoring during physical activity, a Bluetooth module is integrated into the control module, transmitting acquired signals to user terminals. Machine learning algorithms process the data at the terminal to evaluate current exercise load and provide personalized fitness recommendations.

Figure 1e shows the process of machine learning module building. After the three sets (PENG, TEG, and sEMG) of 200-second data are obtained by personal terminal, each segment is divided into 60 slices of 3 s duration. Then, 12 feature values (mean, variance, standard deviation, etc.) are extracted from each slice, and the features from the 3 types of signal slices in the same period are combined to form a feature matrix. Finally, the Principal Component Analysis (PCA) algorithm is employed to perform dimensionality reduction on the feature array and establish a mapping relationship with exercise intensity.

Pulse signal is one of the fundamental vital signs of the human body and serves as a crucial indicator of exercise intensity. Generally, as exercise intensity increases, the frequency of pulse signals, i.e., heart rate, will correspondingly rise. For those who have long lacked exercise and those who have exercised sufficiently, there exists a significant difference in terms of both

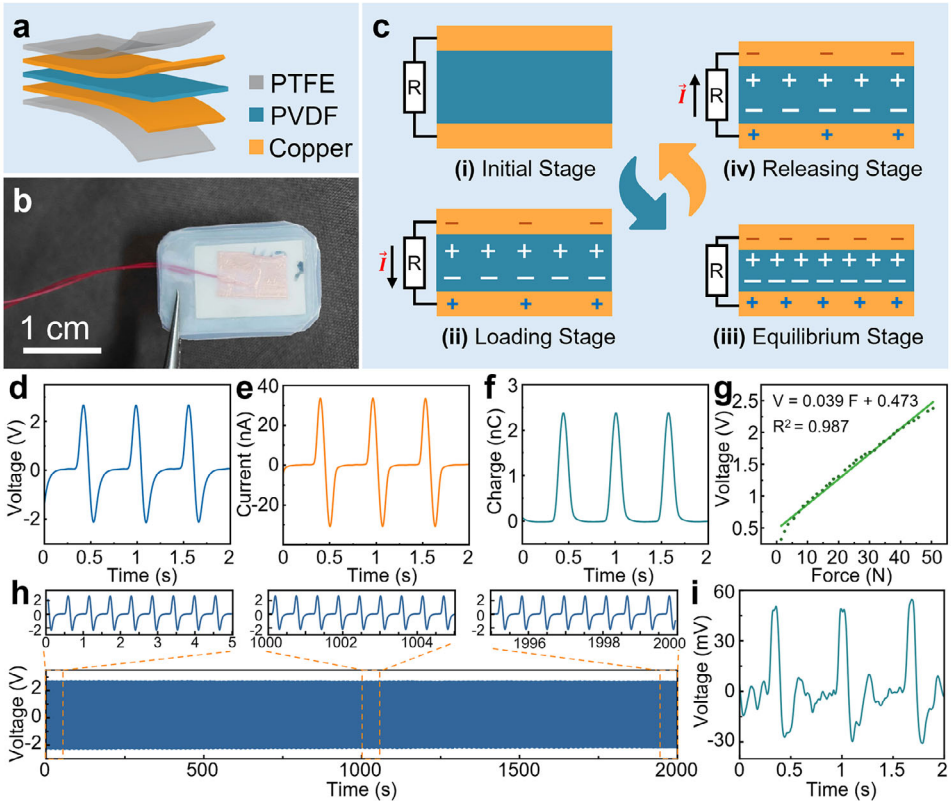

FIGURE 2 | Performance demonstration of the PENG part. (a) The structure design and materials selection of the PENG sensor. (b) Physical picture of PENG. (c) The working principle of PENG. (d–f) The open circuit voltage, short circuit current, and charge transfer under periodic pressure driving, respectively. (g) The fitting curve of open circuit voltage changing with pressure. (h) Steady signal status over 3600 cycles. (i) Signal when monitoring wrist pulse in quiet status.

the acceleration rate of heart rate and the final stabilized heart rate when performing exercises of identical intensity. These physiological signals can effectively guide whether the test subjects have achieved adequate training. MEIAW employs a PENG with superior electromechanical transduction characteristics to acquire both pulsatile and kinematic signals. The PENG module features a five-layer thin-film sandwich architecture (Figure 2a), where PVDF film is selected as the piezoelectric layer due to its pronounced piezoelectric response. Electrodes with pre-bonded lead wires are secured on both surfaces of the PVDF film, followed by polytetrafluoroethylene (PTFE) encapsulation. The PENG sensor is shown in Figure 2b.

The working principle of PENG is illustrated in Figure 2c. Based on the state variations of PENG during its operational cycle, one complete cycle can be divided into four distinct stages. i) Initial stage: The piezoelectric layer maintains electrical neutrality in the absence of external forces. ii) Loading stage: Mechanical strain induced by external force on the PVDF piezoelectric film triggers redistribution of internal dipoles, generating bound charges on its surfaces. The electrodes exhibit positive/negative polarity through electrostatic induction, accompanied by charge flow in the external circuit. iii) Equilibrium stage: Progressive deformation increases the induced charges until maximum strain under applied force is achieved. The system reaches piezoelectric equilibrium, terminating charge transfer. iv) Releasing stage: Upon force removal, charges initiate reverse migration with inverted current polarity until complete restoration to (i) the initial state, awaiting the next cycle. The high responsivity of the piezoelectric film enables the detection of minute skin deformations caused by arterial pulsations, thereby realizing non-invasive pulse monitoring.

Figure 2d–f respectively present the open-circuit voltage (V_{OC}), short-circuit current (I_{SC}), and charge transfer quantity (Q) of the PENG. Under 1.8 Hz mechanical excitation, PENG demonstrates stable performance with V_{OC} peaking at 2.6 V, I_{SC} reaching 61 nA, and Q attaining 2.4 nC. Under applied forces ranging from 0 to 50 N, this PENG demonstrates excellent linearity in its open-circuit voltage (Figure 2g). This indicates that the PENG sensor can accurately respond to external forces within the 0 to 50 N range with a sensitivity of 39 mV/N. Experimental results also confirm that the sensor can successfully detect minute mechanical stimuli as low as 0.007 N (Figure S1). Furthermore, after over 3600 compression cycles under identical excitation conditions, the V_{OC} output retains its peak voltage of 2.6 V, demonstrating the operational stability of the PENG module (Figure 2h). In practical deployment, the PENG was affixed to the skin over the radial artery at the wrist, where it accurately captured pulsatile waveforms (i). The measured V_{OC} exceeded 40 mV, with the signal exhibiting not only the primary contraction wave but also clearly identifiable dicrotic waves. This demonstrates the high sensitivity of the PENG module in detecting faint biomechanical signals.

Body temperature variations reflect physical state changes and energy consumption, thus changing with exercise intensity

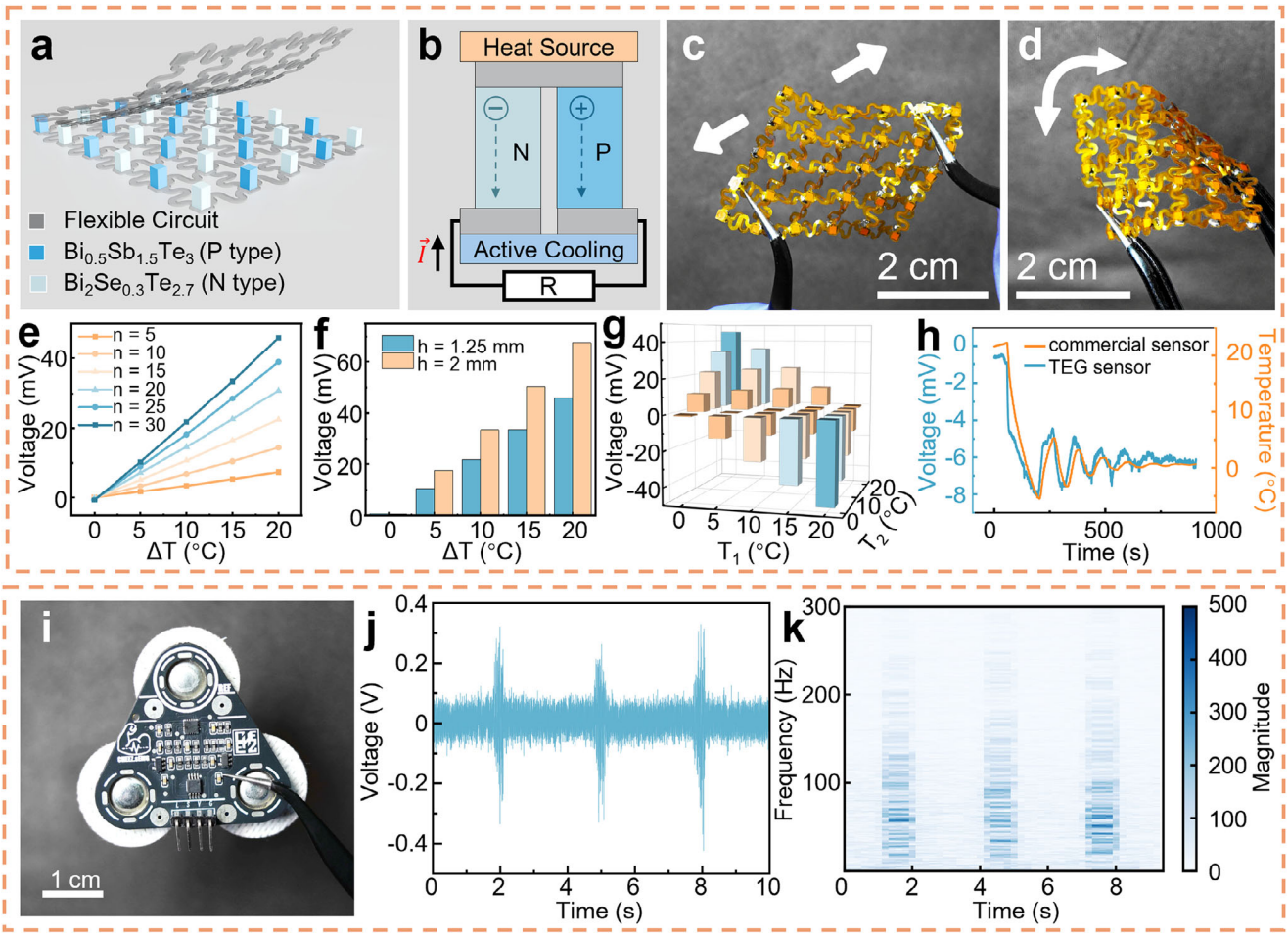

FIGURE 3 | Performance dimensions of the TEG part and the sEMG part. (a) Structure design and materials selection of the TEG sensor. (b) The working principle of TEG. (c,d) demonstrate the tensile and bending performance of TEG sensors, respectively. (e) The trend of V_{OC} variation with ΔT for TEG sensors with varying numbers of units. (f) V_{OC} of TEG sensors at two different heights under different ΔT. (g) V_{OC} of the TEG sensors under varying baseline ΔT. (h) The output signal of the TEG sensor exhibits excellent agreement with commercial references. (i) Physical display of the sEMG module. (j,k) The EMG signal variations and their corresponding frequency spectra induced by three repetitive actions.

during training. For monitoring, a TEG sensor is integrated into the MEIAW. This sensor consists of 15 thermoelectric units composed of $Bi_{0.5}Sb_{1.5}Te_3$ (*p*-type) and $Bi_2Se_{0.3}Te_{2.7}$ (*n*-type) thermoelectric legs (1 ×1 ×2 mm), which are interconnected via serpentine-shaped PI-based flexible printed circuits (FPC) (Figure 3a). The working principle of the thermoelectric unit is shown in Figure 3b. Temperature gradients between terminals drive carrier migration toward cooler regions, establishing potential differences that induce charge circulation through the external circuit. Serpentine design of the FPC enhances stretchability and torsional compliance (Figure 3c,d), enabling better skin conformity to ensure temperature monitoring accuracy.

Figure 3e illustrates the correlation between the output voltage, the quantity of thermoelectric legs, and temperature gradients. When the cold junction is stabilized at 0°C, the voltage output increases as the temperature gradient increases. This is because the increased temperature gradient enhances the carrier mobility within the semiconductor, thereby amplifying the potential difference. Under identical temperature gradients, series-interconnected configurations enable additive superposition of individual potential differences generated across each semiconductor block operating under a temperature gradient. As a result, the sensitivity of the device can reach 2.33 mV K^{-1}. The output performances of thermoelectric legs with two different heights (2 and 1.25 mm) are compared in Figure 3f. For thermoelectric legs with a length of 2 mm, the extended heat transfer path length between hot and cold ends reduces thermal conduction, facilitating more stable temperature differential establishment and maintenance, thereby achieving 67.5 mV output voltage—a 47% increase over the 1.25-mm legs. Meanwhile, the consistency of charge mobility under the same thermal gradient conditions was verified. Figure 3e,f further demonstrate the TEG sensor's linear response and reliable detection capability to temperature differences spanning 0 to 20°C, confirming its competence for accurate body temperature monitoring across diverse environments. Figure 3g presents the V_{OC} characteristics of the TEG module under differential temperature conditions (T_1 and $T_2 \in [0, 20]$°C) applied to its respective surfaces. The output voltages demonstrate essential consistency when |ΔT| values remain equivalent, evidencing the temperature detection capability of the TEG module across varied ambient temperature conditions. Finally, the performance of the TEG module is compared with that of a commercial sensor to verify its measurement accuracy

(Figure 3h). The voltage curve output from the TEG module exhibits remarkable similarity to the temperature profile recorded by commercial sensors, with nearly identical variation trends. Moreover, it is experimentally demonstrated that the module responds to temperature changes as small as 0.1°C at room temperature (23°C), as shown in Figure S2. This demonstrates the high accuracy of the TEG module in temperature measurement, particularly in tracking temperature variation patterns.

The sEMG signals can reflect muscle fatigue levels, which in turn indicate exercise intensity. Figure 3i shows the physical diagram of the sEMG module. The module is attached to the skin over the extensor carpi ulnaris muscle and flexor digitorum superficialis muscle on the forearm using adhesive wet electrodes. When muscle activity occurs, the sensor detects fluctuations in sEMG signals (action potentials) (Figure 3j). The spectral analysis of these signals (Figure 3k) shows that the main frequency signal interval of the three motion signals is 3 s, which exactly corresponds to the period between the predetermined continuous motions in the test.

To distinguish and assess different levels of fatigue, PCA was employed to process and analyze multimodal data from physical exercise. PCA is the most widely used algorithm for data dimensionality reduction. The principle of PCA is to map n-dimensional features onto k-dimensional features, which are new orthogonal features also known as principal components.

To ensure movement standardization, experimental consistency, and operational convenience, all five participants were instructed to securely and consistently wear the MEIAW wristband following the protocol illustrated in Figure 1b. Participants were required to use a hand dynamometer calibrated at 20 kg, with each grip requiring full compression to the mechanical endpoint of the device. They subsequently performed standardized gripping motions at 2-second intervals until reaching task-terminating muscle fatigue, enabling comprehensive physiological monitoring from full vitality to complete exhaustion. This protocol facilitated continuous acquisition of pulse rhythm, body temperature fluctuations, and sEMG signals throughout the complete exercise cycle. As the number of movements increased, the level of fatigue in the subjects also gradually increased. Therefore, to facilitate quantitative analysis of fatigue levels, we define the fatigue level at the first movement (the start of the exercise) as 0, representing the state of minimal fatigue. The fatigue level at the last successful repetition of the standard movement (before fatigue prevents the completion of the standard movement) is defined as 1, representing the maximum fatigue for that individual in the task. We assume that fatigue accumulates linearly with the number of repetitions completed (or the time elapsed) between these two endpoints. Thus, the normalized fatigue level at any intermediate point n (where n is the number of repetitions between 1 and N_{max}, the final repetition) is calculated as follows:

$$\text{Normalized Fatigue Level} = \frac{n}{N_{max}} \quad (1)$$

Data were collected from over 50 consecutive periodic movements performed by the subjects (Figure 4a; Figure S3). First, these three types of signals are segmented according to the action cycle, so that each segment represents the signal of one action cycle, and then features are extracted from these segments. These features include Standard Deviation (STD), Entropy (Ent), Autocorrelation Coefficient (AC), Zero Cross Rate (ZCR), Power, Root Mean Square (RMS, the RMS of TEG is shown in Figure 4b), Sum, Peak-to-Peak Value (PPV), Peak-Valley Interval (PVI), Kurtosis (KUR), Skewness (SKE), and Mean Power Frequency (MPF), they are shown in Figure S4, and the relevant calculation formulas are also recorded in Note 1.

Figure 4c–e present scatter plots of feature dimensionality reduction for individual signals (pulse, sEMG and body temperature), with the horizontal and vertical axes representing Principal Component 1 and Principal Component 2, respectively; as dimensionality reduction integrates multiple features, these principal components lack straightforward physical interpretations, and although color-coding indicates fatigue levels, Figure 4c,d show no discernible pattern between scatter distribution and color gradients, while Figure 4e exhibits significant point clustering that impedes differentiation of intermediate fatigue states, thus indicating that utilizing individual signals for fatigue assessment suffers from inadequate discriminative capability; in contrast, Figure 4f demonstrates the dimensionality reduction results for hybrid signals, where the scatter distribution establishes a clearly defined, near-linear relationship with color gradients, confirming hybrid signals' superior discriminative power for fatigue level identification. Among the numerous features mentioned above, different features contribute differently to the model construction, and Figure 4g illustrates their respective contribution proportions (in the figure, "PENG Power" denotes the Power feature of PENG, and so forth for other feature naming conventions).

Here, to practically validate the feasibility of multimodal sensing, the MEIAW was employed to monitor physiological states during physical exercise. The working positions and corresponding physiological signals source of each component of the MEIAW are shown in Figure 5a. The MEIAW was worn throughout the entire exercise session, with pulse, body temperature, and EMG signals during the initial, middle, and fatigue stages displayed in Figure 5b. It can be clearly seen that as the exercise continues, the pulse increases from 77.60 bpm in the initial stage to 91.04 bpm in the fatigue stage (subgraphs (1), (2), and (3) in Figure 5b). Meanwhile, body temperature increased from 35.3°C (initial phase) to 35.9°C (middle phase) and subsequently stabilized (subgraphs (4), (5), and (6) in Figure 5b). This steady temperature state reflects the body's compensatory mechanisms to enhance heat dissipation and maintain thermal homeostasis, thereby preventing hyperthermia-induced physiological impairment. The sEMG signals of the initial, middle, and fatigue stages of this exercise process are shown in Figure 5b (7), (8), and (9), respectively. By analyzing the characteristic features of these physiological signals, we can effectively assess the user's real-time exercise status. This analytical framework enables: generation of tailored recommendations matching current exertion levels, and early warnings for persistent overexertion through continuous monitoring (the program flowchart is shown in Figure S5).

Figure 5c,d show the obverse and reverse sides of the printed circuit board (PCB) of the control module. This compact 40 × 30 mm PCB integrates a PENG signal processor, EMG processor,

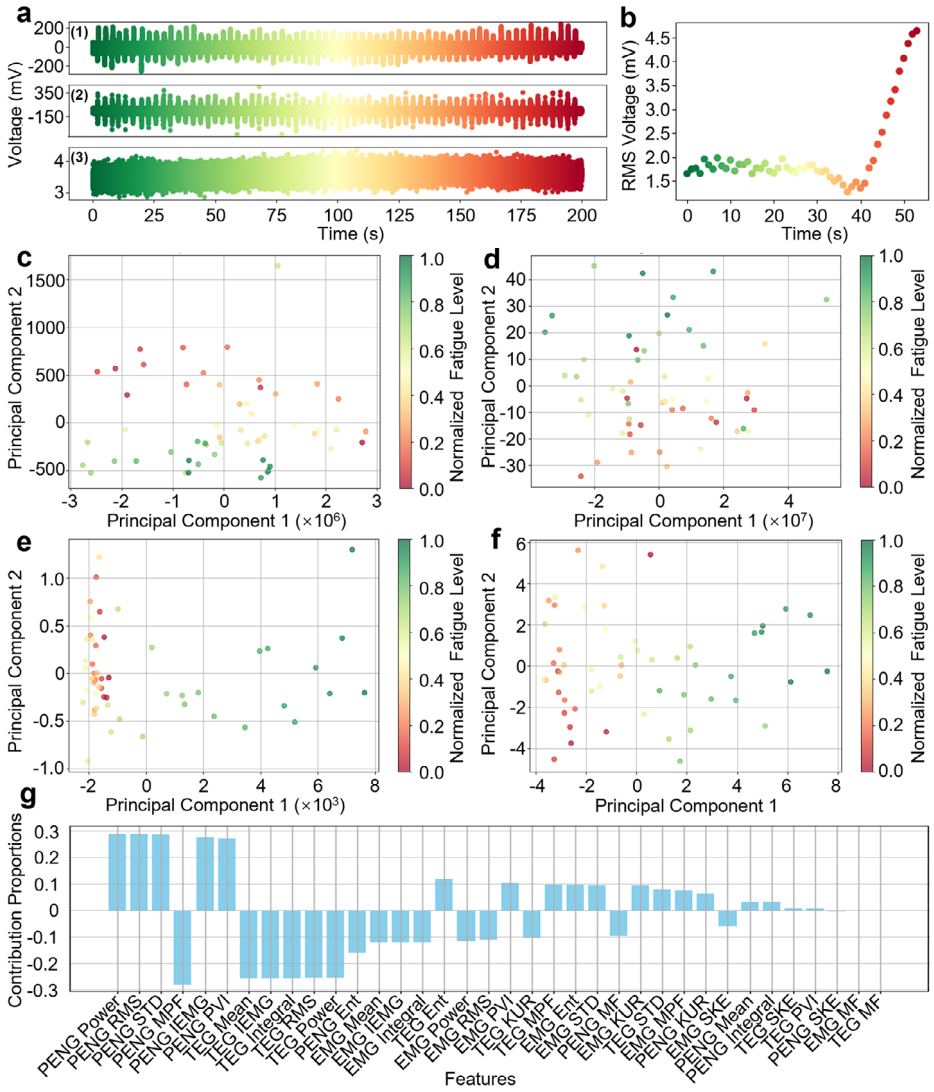

FIGURE 4 | Signal processing results during machine learning. (a) Time series diagram of (1) pulse, (2) sEMG, and (3) body temperature during exercise. (b) Root mean square of the pulse signal. Dimensionality reduction scatter mapping diagram of (c) pulse, (d) sEMG, (e) body temperature, and (f) hybrid signal. (g) The contribution of each feature value to the model among the three signals.

TEG signal processor, power controller, and data storage module to achieve preliminary signal processing, power management, and data storage functionalities. The wiring diagrams of the PCB's obverse and reverse sides are presented in Figure 5e (1) and (2), respectively. In addition, the schematic diagram of the PCB is also provided in Figure S6.

3 | Conclusions and Discussion

In conclusion, since pulse rate, body temperature, and muscle fatigue levels serve as critical references for assessing exercise intensity, a multimodal wristband based on PENG, TEG, and sEMG technologies is developed to function as an exercise assistant for physical training reference. In the MEIAW system, leveraging responsiveness to mechanical signals of PENG, a PVDF-film-based piezoelectric sensor is fabricated for pulse monitoring. Utilizing the high thermal sensitivity of TEG, a TEG module was developed using $Bi_{0.5}Sb_{1.5}Te_3$ and $Bi_2Se_{0.3}Te_{2.7}$ thermoelectric legs to track body temperature variations. Additionally, sEMG signals were acquired to assess muscle fatigue levels. By integrating these three sensors and incorporating machine learning techniques, a comprehensive evaluation of exercise intensity was achieved. The heart rate, body temperature, and sEMG of the subject were continuously monitored during a single session of continuous physical exercise. The heart rate increased from 70 to 80, body temperature rose from 36.1 to 36.9, and continuous changes in electromyography were also recorded. This provides exercisers with objective, individualized exercise recommendations based on physiological characteristics. The present study may serve as a reference for intelligent physiological health monitoring in the future.

4 | Experimental Section

4.1 | Materials

PVDE was purchased from VKING Manufacturing Co., Ltd. The PCB and FPC using LCEDA-pro was designed, and the

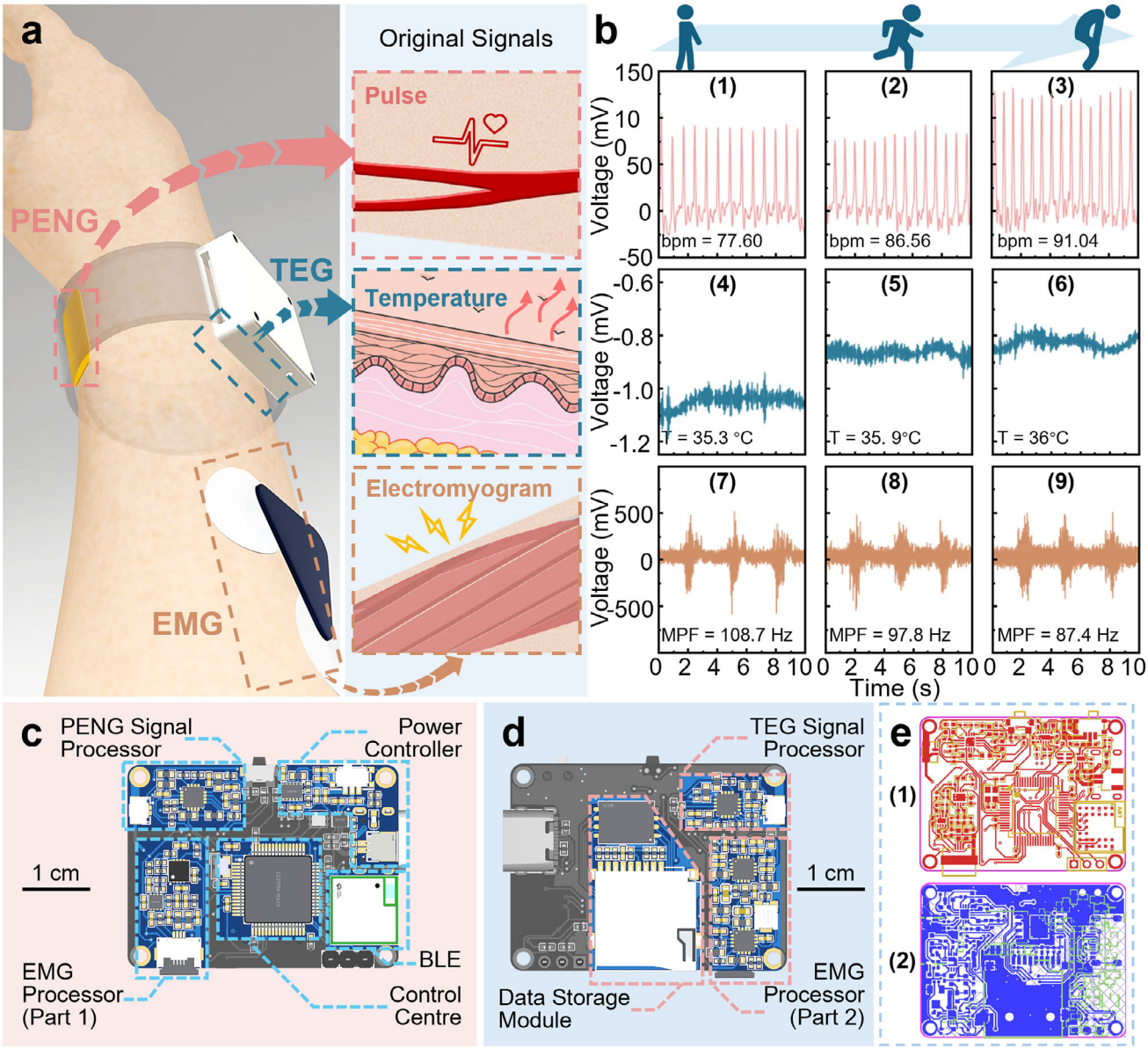

FIGURE 5 | Application demonstration of the MEIAW. (a) These three sensors and the raw signals they monitor. (b) The signals of the MEIAW during the initial, middle, and fatigue stages of exercise. (c,d) respectively display the front and back sides of the control module PCB for the MEIAW with integrated functional modules. (e) Wiring diagrams for the front and back of the control module.

PCB manufacturing service was provided by Shenzhen JLC Technology Group Co., Ltd. The 3D resin casing was designed using FreeCAD, and the 3D printing service was provided by Shenzhen JLC Technology Group Co., Ltd. The $Bi_{0.5}Sb_{1.5}Te_3$ and $Bi_2Se_{0.3}Te_{2.7}$ thermoelectric legs were purchased from Quanzhou Qijin New Material Co., Ltd.

4.2 | Fabrication

1) Preparation of the PENG sensor. First, a 50-micron-thick PVDF film was cut into 1 cm × 1.5 cm pieces. Copper foil was then attached to both sides of the PVDF, and wires were drawn out. Encapsulation was performed using a 0.1 mm-thick PTFE film. 2) Preparation of the TEG sensor. First, low-temperature solder paste was evenly applied to the pads of a pair of FPCs. N-type and *p*-type TE legs were alternately placed on the solder-pasted pads. Finally, a hot plate was used to melt the solder paste, fully filling the gaps between the pads and TE legs. After cooling, the TEG sensor was obtained. 3) Integration. The prepared PENG sensor, TEG sensor, sEMG module, and PCB of the control module were assembled, ultimately yielding the MEIAW prototype with a total mass of 31 g (excluding wrist strap components).

4.3 | Characterization and Measurement

The linear motor (LinMot E1100) was used to continuously provide periodic pressure to the PENG sensor. A Keithley 6517 electrometer is employed to measure the charge transfer, V_{OC}, and I_{SC} of both the PENG sensor and TEG sensor, while an oscilloscope (LeCroy HDO6104) was used to acquire and record

the data. A self-made temperature control platform based on the Peltier effect was utilized to provide a stable temperature gradient for measuring the relevant performance of the TEG sensor.

This work has been approved by the Medical Ethics Review Committee of the Beijing Institute of Nanoenergy and Nanosystems, with the ethics approval number 2025012LZ.

Author Contributions

Puchuan Tan, **Yang Zou**, **Aihua Liang**, **Guanlin Lin**, and **Zhou Li** supervised the project and designed the experiment. **Puchuan Tan**, **Aihua Liang**, **Guanlin Lin**, and **Zhou Li** provided financial support and guidance for the project. **Daiwu Shen**, **Puchuan Tan**, **Yuan Xi**, and **Cong Li** conducted experiments, data processing, and data analyses. **Daiwu Shen**, **Puchuan Tan**, **Yuan Xi**, and **Zhou Li** wrote and proofread the paper. **Daiwu Shen** and **Puchuan Tan** took and processed the experimental photograph. All authors reviewed and commented on the manuscript.

Acknowledgements

This study was supported by National Key R&D project from Minister of Science and Technology (2022YFB3804700), the National Natural Science Foundation of China (T2125003), China Postdoctoral Science Foundation (2023M743446), Beijing Natural Science Foundation (L245015), the Fundamental Research Funds for the Central Universities, CACMS Innovation Fund (CI2023C006YG), State Key Laboratory for Quality Ensurance and Sustainable Use of Dao-di Herbs (ZG2024001-03), Qihuang Scholar Program. Meanwhile, this study also received technical support provided by Yueheng Weng. The authors were grateful to all the laboratory members for their cooperation in this study.

Conflicts of Interest

The authors declare no conflicts of interest.

Data Availability Statement

The data that support the findings of this study are available from the corresponding author upon reasonable request.

References

1. M. C. Löffler, M. J. Betz, D. P. Blondin, et al., "Challenges in Tackling Energy Expenditure as Obesity Therapy: From Preclinical Models to Clinical Application," *Molecular Metabolism* 51 (2021): 101237.

2. L. Chen, D. J. Magliano, and P. Z. Zimmet, "The Worldwide Epidemiology of Type 2 Diabetes Mellitus—Present and Future Perspectives," *Nature Reviews Endocrinology* 8 (2012): 228–236.

3. L. Lara-Castor, M. O'Hearn, F. Cudhea, et al., "Burdens of Type 2 Diabetes and Cardiovascular Disease Attributable to Sugar-Sweetened Beverages in 184 Countries," *Nature Medicine* 31 (2025): 552–564.

4. Z. Chen, D. Guo, L. Xiao, H. Su, and Y. Chen, "Association of Fat-to-Muscle Ratio With hypertension: A Cross-Sectional Study in China," *Journal of Human Hypertension* 39 (2025): 301–307.

5. J. Lu, Y. Lu, X. Wang, et al., "Prevalence, Awareness, Treatment, and Control of Hypertension in China: Data From 1·7 Million Adults in a Population-Based Screening Study (China PEACE Million Persons Project)," *The Lancet* 390 (2017): 2549–2558.

6. E. Reisin and A. V. Jack, "Obesity and Hypertension: Mechanisms, Cardio-Renal Consequences, and Therapeutic Approaches," *Medical Clinics of North America* 93 (2009): 733–751.

7. Y. Zhao, M. Chukanova, K. A. Kentistou, et al., "Protein-Truncating Variants in BSN are Associated With Severe Adult-Onset Obesity, Type 2 Diabetes and Fatty Liver Disease," *Nature Genetics* 56 (2024): 579–584.

8. G. Bedogni, S. Bellentani, L. Miglioli, et al., "The Fatty Liver Index: A Simple and Accurate Predictor of Hepatic Steatosis in the General Population," *BMC Gastroenterology* 6 (2006): 33.

9. M. Blüher, "Obesity: Global Epidemiology and Pathogenesis," *Nature Reviews Endocrinology* 15 (2019): 288–298.

10. G. A. Bray, K. K. Kim, J. P. H. Wilding, and World Obesity Federation, "Obesity: A Chronic Relapsing Progressive Disease Process. A Position Statement of the World Obesity Federation," *Obesity Reviews* 18 (2017): 715–723.

11. J. Geng, X. Zhang, Y. Guo, et al., "Moderate-Intensity Interval Exercise Exacerbates Cardiac Lipotoxicity in High-Fat, High-Calories Diet-Fed Mice," *Nature Communications* 16 (2025): 613.

12. Y. Arino, A. Terashima, T. Tsubaki, et al., "Short-Term Overloading Exercise Attenuates Articular Chondrocyte Features Partly via Synovium–Cartilage Interactions Mediated by Inhibin Subunit Beta A," *Scientific Reports* 15 (2025): 6772.

13. S. H. Chang, D. Mori, H. Kobayashi, et al., "Excessive Mechanical Loading Promotes Osteoarthritis Through the Gremlin-1–NF-κB Pathway," *Nature Communications* 10 (2019): 1442.

14. J. G. Do, S. U. Noh, S. W. Chae, K. J. Yoon, and Y.-T. Lee, "Excessive Walking Exercise Precipitates Diabetic Neuropathic Foot Pain: Hind Paw Suspension Treadmill exercise Experiment in a Rat Model," *Scientific Reports* 10 (2020): 10498.

15. Y. BaiQuan, C. Meng, Z. Congqing, and W. XiaoDong, "The Effects and Post-Exercise Energy Metabolism Characteristics of Different High-Intensity Interval Training in Obese Adults," *Scientific Reports* 15 (2025): 13770.

16. Y. Schutz, "Respiration Chamber Calorimetry and Doubly Labeled Water: Two Complementary Aspects of Energy Expenditure?," *European Journal of Clinical Nutrition* 72 (2018): 1310–1313.

17. D. A. Schoeller, E. Ravussin, Y. Schutz, K. J. Acheson, P. Baertschi, and E. Jéquier, "Energy Expenditure by Doubly Labeled Water: Validation in Humans and Proposed Calculation," *American Journal of Physiology* 250 (1986): R823–R830.

18. E. Jéquier and Y. Schutz, "Long-Term Measurements of Energy Expenditure in Humans Using a Respiration Chamber," *The American Journal of Clinical Nutrition* 38 (1983): 989–998.

19. Z. L. Wang and J. Song, "Piezoelectric Nanogenerators Based on Zinc Oxide Nanowire Arrays," *Science* 312 (2006): 242–246.

20. X. Chen, J. Shao, N. An, et al., "Self-Powered Flexible Pressure Sensors With Vertically Well-Aligned Piezoelectric Nanowire Arrays for Monitoring Vital Signs," *Journal of Materials Chemistry C* 3 (2015): 11806–11814.

21. D. H. Kim, H. J. Shin, H. Lee, et al., "In Vivo Self-Powered Wireless Transmission Using Biocompatible Flexible Energy Harvesters," *Advanced Functional Materials* 27 (2017): 1700341.

22. A. Wang, Z. Liu, M. Hu, et al., "Piezoelectric Nanofibrous Scaffolds as In Vivo Energy Harvesters for Modifying Fibroblast Alignment and Proliferation in Wound Healing," *Nano Energy* 43 (2018): 63–71.

23. F.-R. Fan, Z.-Q. Tian, and Z. L. Wang, "Flexible Triboelectric Generator," *Nano Energy* 1 (2012): 328–334.

24. F.-R. Fan, L. Lin, G. Zhu, W. Wu, R. Zhang, and Z. L. Wang, "Transparent Triboelectric Nanogenerators and Self-Powered Pressure Sensors Based on Micropatterned Plastic Films," *Nano Letters* 12 (2012): 3109–3114.

25. G. Zhu, C. Pan, W. Guo, et al., "Triboelectric-Generator-Driven Pulse Electrodeposition for Micropatterning," *Nano Letters* 12 (2012): 4960–4965.

26. S. Patel, H. Park, P. Bonato, L. Chan, and M. Rodgers, "A Review of Wearable Sensors and Systems With Application in Rehabilitation," *Journal of NeuroEngineering and Rehabilitation* 9 (2012): 21.

27. B. C.-K. Tee, C. Wang, R. Allen, and Z. Bao, "An Electrically and Mechanically Self-Healing Composite With Pressure- and Flexion-Sensitive Properties for Electronic Skin Applications," *Nature Nanotechnology* 7 (2012): 825–832.

28. F. J. DiSalvo, "Thermoelectric Cooling and Power Generation," *Science* 285 (1999): 703–706.

29. W. Shin, M. Matsumiya, F. Qiu, N. Izu, and N. Murayama, "Thermoelectric Gas Sensor for Detection of High Hydrogen Concentration," *Sensors and Actuators B: Chemical* 97 (2004): 344–347.

30. F. Rettig and R. Moos, "α-Iron Oxide: An Intrinsically Semiconducting Oxide Material for Direct Thermoelectric Oxygen Sensors," *Sensors and Actuators B: Chemical* 145 (2010): 685–690.

31. D. M. Ackermann, E. L. Foldes, N. Bhadra, and K. L. Kilgore, "Nerve Conduction Block using Combined Thermoelectric Cooling and High Frequency Electrical stimulation," *Journal of Neuroscience Methods* 193 (2010): 72–76.

32. E. Miyako, C. Hosokawa, M. Kojima, et al., "A Photo-Thermal-Electrical Converter Based On Carbon Nanotubes for Bioelectronic Applications," *Angewandte Chemie International Edition* 50 (2011): 12266–12270.

33. H. Ouyang, Z. Liu, N. Li, et al., "Symbiotic Cardiac Pacemaker," *Nature Communications* 10 (2019): 1821.

34. Z. Che, S. O'Donovan, X. Xiao, et al., "Implantable Triboelectric Nanogenerators for Self-Powered Cardiovascular Healthcare," *Small* 19 (2023): 2207600.

35. Q. Zheng, B. Shi, F. Fan, et al., "In Vivo Powering of Pacemaker by Breathing-Driven Implanted Triboelectric Nanogenerator," *Advanced Materials* 26 (2014): 5851–5856.

36. W. Sun, J. Xue, P. Tan, B. Shi, Y. Zou, and Z. Li, "A Self-Powered Multifunctional Bracelet for Pulse Monitoring and Personal Rescue," *Biosensors* 13 (2023): 552.

37. J. Dai, J. Meng, X. Zhao, et al., "A Wearable Self-Powered Multi-Parameter Respiration Sensor," *Advanced Materials Technologies* 8 (2023): 2201535.

38. Y. Zhang, L. Xu, Z. Liu, et al., "Self-Powered Pulsed Direct Current Stimulation System for Enhancing Osteogenesis in MC3T3-E1," *Nano Energy* 85 (2021): 106009.

39. H. Ning, W. Zhou, L. Tuo, et al., "Tensegrity Triboelectric Nanogenerator for Broadband Blue Energy Harvesting in All-Sea Areas," *Nano Energy* 117 (2023): 108906.

40. X. Hu, J. Feng, C. Liang, et al., "Round-Trip Oscillation Triboelectric Nanogenerator With High Output Response and Low Wear to Harvest Random Wind Energy," *Nano Research* 16 (2023): 11259–11268.

41. Y. Jung, J. Choi, Y. Yoon, H. Park, J. Lee, and S. H. Ko, "Soft Multi-Modal Thermoelectric Skin for Dual Functionality of Underwater Energy Harvesting and Thermoregulation," *Nano Energy* 95 (2022): 107002.

42. M. Zadan, A. Wertz, D. Shah, et al., "Stretchable Thermoelectric Generators for Self-Powered Wearable Health Monitoring," *Advanced Functional Materials* 34 (2024): 2404861.

43. X. Zhang, S. Tang, R. Ma, et al., "High-Performance Multimodal Smart Textile for Artificial Sensation and Health Monitoring," *Nano Energy* 103 (2022): 107778.

44. M. Xu, S. Wang, S. L. Zhang, et al., "A Highly-Sensitive Wave Sensor Based on Liquid-Solid Interfacing Triboelectric Nanogenerator for Smart Marine Equipment," *Nano Energy* 57 (2019): 574–580.

45. J. Yu, X. Hou, J. He, et al., "Ultra-Flexible and High-Sensitive Triboelectric Nanogenerator as Electronic Skin for Self-Powered Human Physiological Signal Monitoring," *Nano Energy* 69 (2020): 104437.

46. J. B. Park, M. S. Song, R. Ghosh, et al., "Highly Sensitive and Flexible Pressure Sensors using Position- and Dimension-Controlled ZnO Nanotube Arrays Grown on Graphene Films," *NPG Asia Mater* 13 (2021): 57.

47. Y. Cao, Y. Guo, Z. Chen, et al., "Highly Sensitive Self-Powered Pressure and Strain Sensor Based on Crumpled MXene Film for Wireless Human Motion Detection," *Nano Energy* 92 (2022): 106689.

48. K. K. Kim, J. Bang, M. Kim, J. Jeong, I. Ha, and S. H. Ko, "Unisensory Processing of Interleaving Memristive Nanowires Enabling Multimodal Sensing at Human-Scale Resolution," *Nature Materials* (2025).

49. J. J. Park, S. Hong, Y. Jung, et al., "Highly Sensitive Cuffless Blood Pressure Monitoring With Selective Laser-Sintered Liquid Metal Conductors," *Advanced Functional Materials* 35 (2025): 2505089.

50. H. Park, S. Yoon, J. Bang, et al., "A Deep-Learned Monolithic Nanoparticle Asymmetric Thermal Flow Sensor for Flow Vector Estimation," *ACS Nano* 19 (2025): 30961–30972.

51. Y. Zhang, Z. Li, X. Fan, et al., "A Fully Integrated, Non-Invasive, and Multimodal Wearable Device for Sweat Stimulation, Collection and Multiple Physiological Signals Analysis," *Chemical Engineering Journal* 505 (2025): 159209.

52. Y. Gai, E. Wang, M. Liu, et al., "A Self-Powered Wearable Sensor for Continuous Wireless Sweat Monitoring," *Small Methods* 6 (2022): 2200653.

53. X. Wan, Z. Wang, X. Zhao, et al., "Flexible and Highly Piezoelectric Nanofibers With Organic–Inorganic Coaxial Structure for Self-Powered Physiological Multimodal sensing," *Chemical Engineering Journal* 451 (2023): 139077.

54. K. K. Kim, M. Kim, K. Pyun, et al., "A Substrate-Less Nanomesh Receptor with Meta-Learning for Rapid Hand Task Recognition," *Nature Electronics* 6 (2023): 64–75.

55. K. R. Pyun, K. Kwon, M. J. Yoo, et al., "Machine-Learned Wearable Sensors for Real-Time Hand-Motion Recognition: Toward Practical Applications," *National Science Review* 11 (2024): nwad298.

56. K. K. Kim, I. Ha, M. Kim, et al., "A Deep-Learned Skin Sensor Decoding the Epicentral Human Motions," *Nature Communications* 11 (2020): 2149.

57. P. Won, J. J. Park, T. Lee, et al., "Stretchable and Transparent Kirigami Conductor of Nanowire Percolation Network for Electronic Skin Applications," *Nano Letters* 19 (2019): 6087–6096.

58. Y. Jung, M. Kim, S. Jeong, S. Hong, and S. H. Ko, "Strain-Insensitive Outdoor Wearable Electronics by Thermally Robust Nanofibrous Radiative Cooler," *ACS Nano* 18 (2024): 2312–2324.

59. J. Shin, B. Jeong, J. Kim, et al., "Sensitive Wearable Temperature Sensor With Seamless Monolithic Integration," *Advanced Materials* 32 (2020): 1905527.

60. K. K. Kim, J. Choi, J.-H. Kim, S. Nam, and S. H. Ko, "Evolvable Skin Electronics by In Situ and In Operando Adaptation," *Advanced Functional Materials* 32 (2022): 2106329.

61. D. Won, J. Kim, J. Choi, et al., "Digital Selective Transformation and Patterning of Highly Conductive Hydrogel Bioelectronics by Laser-Induced Phase Separation," *Science Advances* 8 (2022): abo3209.

62. D. Won, H. Kim, J. Kim, et al., "Laser-Induced Wet Stability and Adhesion of Pure Conducting Polymer Hydrogels," *Nature Electronics* 7 (2024): 475–486.

63. D. Kim, J. Bang, P. Won, et al., "Biocompatible Cost-Effective Electrophysiological Monitoring With Oxidation-Free Cu–Au Core–Shell Nanowire," *Advanced Materials Technologies* 5 (2020): 2000661.

64. H. Yoon, J. Choi, J. Kim, et al., "Adaptive Epidermal Bioelectronics by Highly Breathable and Stretchable Metal Nanowire Bioelectrodes on Electrospun Nanofiber Membrane," *Advanced Functional Materials* 34 (2024): 2313504.

65. J. Kim, D. Won, T. H. Kim, C.-Y. Kim, and S. H. Ko, "Rapid Prototyping and Facile Customization of Conductive Hydrogel Bioelectronics Based on All Laser Process," *Biosensors and Bioelectronics* 258 (2024): 116327.

66. D. Kim, J. Lee, M. K. Park, and S. H. Ko, "Recent Developments in Wearable Breath Sensors for Healthcare Monitoring," *Communications Materials* 5 (2024): 41.

67. Y. Jung, K. R. Pyun, S. Yu, et al., "Laser-Induced Nanowire Percolation Interlocking for Ultrarobust Soft Electronics," *Nano-Micro Letters* 17 (2025): 127.

68. K. Y. Kim, J. Kang, S. Song, et al., "An Ultrathin Organic–Inorganic Integrated Device for Optical Biomarker Monitoring," *Nature Electronics* 7 (2024): 914–923.

Supporting Information

Additional supporting information can be found online in the Supporting Information section.

Supporting file: admt70708-sup-0001-SuppMat.pdf